

Simultaneous Power Harvesting and Cyclostationary Spectrum Sensing in Cognitive Radios

WON MEE JANG 

Department of Electrical and Computer Engineering, University of Nebraska–Lincoln, Omaha, NE 68182, USA

e-mail: wjang1@unl.edu

ABSTRACT We expect that 5G will support a large volume of data traffic to provide various services with a low latency. This will inevitably require an increased amount of energy. Wireless power transfer needs a higher receiver sensitivity than data decoding. Increased electromagnetic fields may introduce harmful effects on living organisms. Fortunately, massive multiple-input and multiple-output (MIMO) can provide significant gains in radiated energy and spectral efficiencies. Cognitive radio and 5G are emerging technologies. In this paper, we show that cognitive spectrum sensing and power harvesting can be accomplished simultaneously. Energy detection (ED) with energy harvesting has been widely investigated. However, ED may not work at a low signal-to-noise ratio with a harsh signal fluctuation in millimeter-wave in 5G. Therefore, we focus on cyclostationary spectrum sensing in this paper. We show that the maximum likelihood cyclostationary detection that can be used for power harvesting is the power squared. The cyclic power can be conveniently harvested and used for spectrum sensing.


INDEX TERMS Cognitive radios, cyclostationary spectrum sensing, massive MIMO, power harvesting.

I. INTRODUCTION

Devices in the 5G Internet of Things (IoT) consume a large amount of energy. Although there have been many efforts to create power management policies, the sensor nodes' lifetimes still remain a performance bottleneck and make the wide-range deployment of IoT challenging [1], [2]. Regarding limited battery capacity, the wireless power transfer (WPT) technique is suitable for charging the battery [3]. Another promising technique is to harvest power directly from the radio frequency (RF) electromagnetic waves coming from dedicated wireless energy sources that transmit a known amount of energy at specific locations and times, together with the usual information signals by simultaneous wireless information and power transfer (SWIPT) [4], [5]. In general, it is not possible to perform energy harvesting (EH) and information decoding (ID) operations on the same received signal in a SWIPT system, as the EH operation on the RF signal destroys the information content of the signal. Hence, ID and EH are performed by separate receivers, time switching receivers, or power splitting receivers [6]. The schemes are practically appealing since state-of-the-art wireless information and energy receivers are typically

designed to operate separately with different power sensitivities (e.g., -50 dBm for information receivers and -10 dBm for energy receivers) [7]. A 40 dB or higher EH receiver may introduce harmful electromagnetic field (EMF) effects on living organisms. Fortunately, multiple-input and multiple-output (MIMO) WPT has many attractive advantages since the received power increases with the size of the MIMO [8].

Recently, a 5G-based green broadband communication system with SWIPT was proposed to combine wireless information transfer (WIT) and WPT [9]. In addition, a simultaneous cooperative spectrum sensing and EH model was proposed to improve the transmission performance of the multichannel cognitive radio in [10]. The harvested energy in the sensing slot is stored in a rechargeable battery and later used to compensate for the sensing energy loss in the transmission slot in order to guarantee the throughput of the secondary user. The resource allocation of the proposed model is formulated as a class of optimization problem, which maximizes aggregate throughput, harvested energy, and energy efficiency, respectively. On the other hand, a green-energy-powered cognitive sensor network (CSN) with cooperative sensing is investigated in [11]. Energy harvesting from solar, wind, and radio frequency is a promising technique to achieve green communications. The sensing threshold, the sensing time, and the final decision threshold in the fusion center

The associate editor coordinating the review of this manuscript and approving it for publication was Wen Chen .

are optimized to maximize the cognitive sensor’s throughput and improve the utilization efficiency of the harvested energy.

However, 5G architecture will require intelligent spectrum sensing using cognitive radio (CR) that aggregates spectrum bandwidth in small and large cells [12]. One of the key challenges for cellular systems in the millimeter-wave (mmWave) bands is the rapid channel dynamics [13]. Hence, energy detection (ED) may not work at a low signal-to-noise ratio (SNR) with a harsh signal fluctuation. Besides, in advanced ED, a decision threshold for hypothesis testing is often a function of the SNR [14]. Hence, cyclic-feature detection (CD) is useful in CR [15]–[17], especially at a low SNR. The cyclic spectral density (CSD) was recently used for spectrum sensing in CR with the primary user (PU) signal cyclic frequency (CF) available to the cognitive user (CU) [18]–[20]. On the other hand, blind CD for spectrum sensing was presented in [21]–[24] based on the theory of the higher-order cyclostationarity [25], [26]. The CSD of the digitally modulated signal, such as binary phase-shift keying (BPSK), quadrature phase-shift keying (QPSK), offset quadrature phase-shift keying (OQPSK) and minimum shift keying (MSK), was obtained for CD [27].

Cognitive radio and 5G are two emerging technologies to meet the heavy mobile data traffic of future wireless networks. The need for more capacity will demand more spectrum resulting in the integration of CR into 5G networks [28]. In upcoming 5G, spectrum efficiency will be achieved by opportunistically reusing the cellular spectrum; and energy efficiency will be achieved by RF energy harvesting of ambient cellular signals and RF power injection [29]. Moreover, massive MIMO will provide significant gains in radiated energy and spectral efficiencies by deploying very large antenna arrays at the base station [30]. However, over 230 scientists from more than 40 countries have expressed their “serious concerns” regarding the ubiquitous and increasing exposure to electromagnetic fields (EMF) already generated by electrical and wireless devices before the additional 5G roll-out which will substantially increase exposure to RF EMF. [31].

To ameliorate the negative EMF effects of 5G and to avoid WPT, we will show that cognitive spectrum sensing and power harvesting can be made simultaneously. Energy harvesting with ED has been widely studied. However, ED requires knowledge of the noise variance which may not be available in the millimeter-wave 5G wireless communication system. It would be difficult to find an accurate SNR with rapid channel dynamics. In this context, ED can no longer be considered to be a reliable spectrum sensing technique; and CD may be the only choice left to us. We will develop the the maximum likelihood (ML) detection output of the cyclostationary digital signal, and show that the ML detection output is indeed the signal power squared regardless of the digital modulation scheme employed in the system. The main contribution of our research is to show that the ML detection output of cyclostationary spectrum sensing can be used for

power harvesting. We will demonstrate that the cyclic power can be conveniently obtained for power harvesting, and used for cyclostationary spectrum sensing. The proposed scheme can be especially useful for 5G with massive MIMO.

In Section II, we explore the ML detection of cyclostationary spectrum sensing. The power squared of ML detection output is presented in Section III for BPSK, QPSK, OQPSK, MSK, and quadrature amplitude modulation (QAM). Section IV proposes a simple method of simultaneous cyclostationary spectrum sensing and power harvesting, and provides corresponding simulation results. Our conclusions are presented in Section V.

II. MAXIMUM LIKELIHOOD DETECTION OF CYCLOSTATIONARY SPECTRUM SENSING

Let us consider the instantaneous autocorrelation of a nonstationary signal $x(t)$ [32]

$$R_x(t, \tau) = E[x(t)x(t - \tau)^*] \tag{1}$$

which is periodic with a period T_0 . The superscript $*$ denotes the complex conjugate operation. Its cyclic autocorrelation function (CAF) at a cyclic frequency α is defined as [33], [34]

$$R_x^\alpha(\tau) \triangleq \frac{1}{T_0} \int_{-T_0/2}^{T_0/2} R_x(t, \tau) e^{-j2\pi\alpha t} dt \tag{2}$$

$$= \lim_{T \rightarrow \infty} \frac{1}{T} \int_{-T/2}^{T/2} x(t)x(t - \tau)^* e^{-j2\pi\alpha t} dt \tag{3}$$

as shown in Appendix A. With the Fourier coefficient function $R_x^\alpha(\tau)$, the Fourier series expansion of the instantaneous autocorrelation can be expressed as

$$R_x(t, \tau) = \sum_{\alpha} R_x^\alpha(\tau) e^{j2\pi\alpha t}. \tag{4}$$

The time-dependent cyclic periodogram is shown as [35]–[37]

$$S_x^\alpha(t, f) = \frac{1}{T} X_T(t, f + \alpha/2) X_T(t, f - \alpha/2)^* \tag{5}$$

where

$$X_T(t, f) = \int_{t-T/2}^{t+T/2} x(u) e^{-j2\pi fu} du. \tag{6}$$

On the other hand, the Fourier transform of the cyclic autocorrelation [38]

$$S_x^\alpha(f) \triangleq \int_{-\infty}^{\infty} R_x^\alpha(\tau) e^{-j2\pi f \tau} d\tau \tag{7}$$

$$= \lim_{T \rightarrow \infty} \frac{1}{T} X_T(f + \alpha/2) X_T(f - \alpha/2)^* \tag{8}$$

is called the cyclic spectral density, where

$$X_T(f) = X_T(0, f). \tag{9}$$

Since cyclic autocorrelation is the time average by nature, fading effects will be relatively well taken care of in cyclostationary spectrum sensing. Therefore, fading parameters are

often not explicitly included in the system model or hypotheses of CD [24], [39]. Each CU needs to make a decision between two hypotheses in order to detect spectrum holes:

$$\begin{cases} H_0 : & y(t) = n(t) \\ H_1 : & y(t) = x(t) + n(t) \end{cases} \quad (10)$$

where the null hypothesis H_0 and the alternative hypothesis H_1 indicate the absence and presence of the PU signal, respectively. The signals $y(t)$ and $x(t)$ are the received signal and the PU's transmitted signal. Noise $n(t)$ is a complex white Gaussian noise process with zero mean and variance σ^2 . Hence, the sufficient statistic of the ML detector in an additive white Gaussian noise (AWGN) channel becomes [20, (3)] [37, (15) and (17)]

$$Y_{ML} = \sum_{\alpha} \int_{-\infty}^{\infty} S_x^{\alpha}(f)^* S_y^{\alpha}(t, f) df. \quad (11)$$

We can see that $S_y^{\alpha}(t, f) = S_n^{\alpha}(t, f)$ under the null hypothesis, which vanishes asymptotically as $T \rightarrow \infty$. Under the alternative hypothesis, the signal component of the ML detection variable can be obtained as

$$Y_s = \sum_{\alpha} \int_{-\infty}^{\infty} S_x^{\alpha}(f)^* S_x^{\alpha}(f) df = \sum_{\alpha} \int_{-\infty}^{\infty} |S_x^{\alpha}(f)|^2 df \quad (12)$$

where the indefinite integral

$$Z(\alpha) \triangleq \int_{-\infty}^{\infty} |S_x^{\alpha}(f)|^2 df \quad (13)$$

is defined as the sum of the cyclic spectral density (SCSD), and Y_s can be expressed as

$$Y_s \triangleq \int_{-\infty}^{\infty} \int_{-\infty}^{\infty} S_x^{\alpha}(f)^* S_x^{\alpha}(f) df d\alpha. \quad (14)$$

Applying the identity of $S_x^{\alpha}(f)$ in (8), we see

$$Y_s = \int_{-\infty}^{\infty} \int_{-\infty}^{\infty} \lim_{T \rightarrow \infty} \frac{1}{T} X_T(f + \alpha)^* X_T(f) \times \lim_{T \rightarrow \infty} \frac{1}{T} X_T(f + \alpha) X_T(f)^* df d\alpha. \quad (15)$$

Using the power spectral density (PSD)

$$S_x(f) = \lim_{T \rightarrow \infty} \frac{1}{T} X_T(f)^* X_T(f) = \lim_{T \rightarrow \infty} \frac{1}{T} |X_T(f)|^2 \quad (16)$$

we find [23]

$$Y_s = \int_{-\infty}^{\infty} S_x(\alpha) \otimes S_x(-\alpha)^* d\alpha \quad (17)$$

where the symbol \otimes indicates the convolution operation. From (13) and (17), we observe that the SCSD

$$Z(\alpha) = S_x(\alpha) \otimes S_x(-\alpha)^* = R_{S_x}(\alpha), \quad (18)$$

where $R_{S_x}(\alpha)$ is the autocorrelation of $S_x(\alpha)$. In conclusion, the SCSD is the autocorrelation of the PSD sampled at $\alpha = n/T_0$. This result greatly simplifies the ML detection of

cyclostationary spectrum sensing. Applying the convolution theorem of the Fourier transform to (18), we observe

$$Z(\alpha) \iff T_0 \sum_{n=-\infty}^{\infty} |R_x(\tau - nT_0)|^2 \quad (19)$$

where the notation \iff denotes the Fourier transform pair. Now we introduce the cumulation of the cyclic spectral density (CCSD) $G(\alpha)$:

$$G(\alpha) \triangleq \int_{-\infty}^{\alpha} Z(\beta) d\beta \quad \text{or} \quad (20)$$

$$Y_s = G(\infty) = T_0 \sum_{n=-\infty}^{\infty} |R_x(nT_0)|^2 \quad (21)$$

$$= T_0 |R_x(T_0)|^2 = T_0 P_p^2 \quad (22)$$

where we assume $R_x(nT_0) = 0$ for $n \neq 0$ for digital communications. The symbol P_p is the average power of the PU signal, and we can find the power squared since the period T_0 is known at the CU site. Hence, we can see that the ML detection output Y_{ML} is the power squared under the alternative hypothesis and vanishes asymptotically under the null hypothesis as $T \rightarrow \infty$.

III. THE POWER SQUARED OF MAXIMUM LIKELIHOOD DETECTION FOR DIGITAL MODULATION

The bit error rate (BER) performance of various digital modulation schemes is thoroughly investigated in the literature. Although cyclostationary spectrum sensing of different digital modulation has been theoretically derived in terms of spectrum correlation in [38], its power harvesting characteristics have not been investigated. In this section, we first mathematically derive the ML detection output of each modulation scheme for cyclostationary spectrum sensing.

A. BINARY PHASE-SHIFT KEYING

The BPSK signal can be defined as

$$x_{BPSK}(t) = \begin{cases} b_k P [t - kT_b] \cos(2\pi f_c t) \\ \text{for } kT_b \leq t \leq (k+1)T_b \end{cases} \quad (23)$$

where $b_k = \pm 1$ is polar data being transmitted in the k^{th} bit interval T_b at the bit rate of $R_b = 1/T_b$. The symbol f_c denotes the carrier frequency, and the pulse is

$$P(t) = \begin{cases} \sqrt{2P_p} & 0 \leq t \leq T_b \\ 0 & \text{elsewhere} \end{cases} \quad (24)$$

with the power of the primary user signal equal to P_p . The PSD of the BPSK can be shown as [40], [41]

$$S_x(f) = \frac{P_p T_b}{2} \text{sinc}^2(\pi T_b(f + f_c)) + \frac{P_p T_b}{2} \text{sinc}^2(\pi T_b(f - f_c) T_b) \quad (25)$$

and its inverse Fourier transform is

$$R_x(t) = P_p \Delta\left(\frac{t}{w}\right) \cos(2\pi f_c t) \quad (26)$$

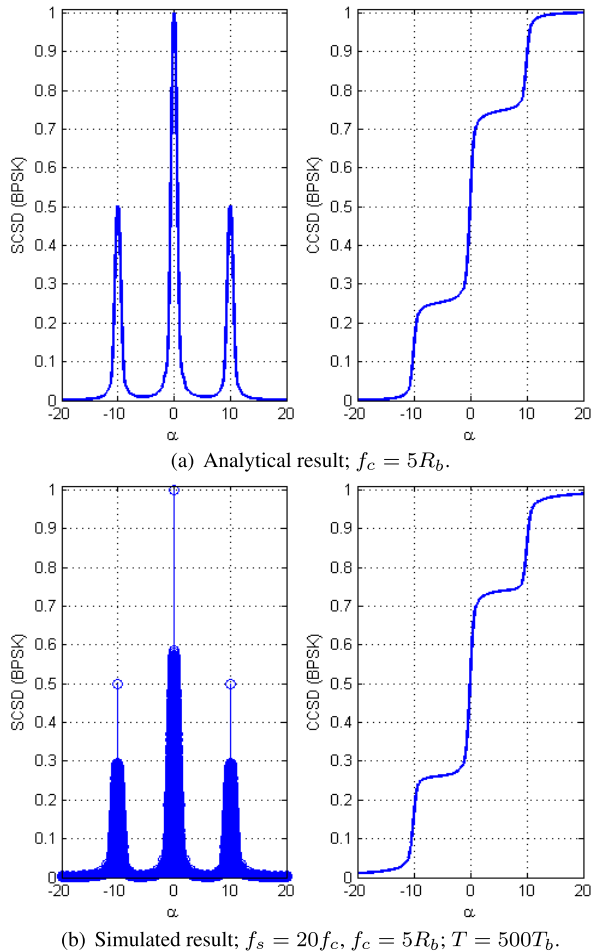


FIGURE 1. SCSD and CCSD of BPSK.

where $w = 2T_b$, and $\Delta(t/w)$ is the triangle of the unit height and the width of w . Since $\Delta^2\left(\frac{t}{2T_b}\right) \iff \Omega_{2T_b}(\alpha)$, as shown in APPENDIX B, replacing T with T_b , we find the SCSD

$$\begin{aligned}
 & T_b \sum_n |R_x(t - nT_b)|^2 \\
 & \iff Z(\alpha) \\
 & = \frac{P_p^2}{2} \Omega_{2T_b}(\alpha) + \frac{P_p^2}{4} \Omega_{2T_b}(\alpha - 2f_c) + \frac{P_p^2}{4} \Omega_{2T_b}(\alpha + 2f_c) \quad (27)
 \end{aligned}$$

and the corresponding ML detection output is

$$G(\infty) = \int_{-\infty}^{\infty} Z(\alpha) d\alpha = T_0 |R_x(T_0)|^2 = T_b P_p^2. \quad (28)$$

The analytical result of SCSD and CCSD of the BPSK are shown in Fig. 1(a). The carrier frequency f_c was chosen to be five times the bit rate for a simple presentation. The SCSD and CCSD were normalized to the peak value, and the cyclic frequency α was normalized to the bit rate. Note that the sizable cyclic power at the CF $\alpha = \pm 2f_c$. Fig. 1(b) shows the simulated result of SCSD and CCSD of the BPSK. The observation interval T was chosen as a 500 bit time. We took samples 20 times in each period of the signal cycle to accurately capture the cyclic property, i.e., the sampling rate $f_s = 20f_c$. We chose the same carrier frequency f_c , equal

to five times the bit rate, for the simulation. The SCSD and CCSD were normalized to the peak value. The simulation results of the SCSD and CCSD agree well with the corresponding analytical results in Fig. 1(a) except the discrete component at $\alpha = 0$ and $\alpha = \pm 2f_c$ due to discrete time processing in the simulation. A similar size of the cyclic power can be observed at the CF $\alpha = \pm 2f_c$ in both analytical and simulated SCSD. Consequently, the same size of jump at the CF can also be observed in both the analytical and simulated CCSD.

B. QUADRATURE PHASE-SHIFT KEYING

The QPSK signal can be defined as

$$x_{QPSK}(t) = \begin{cases} b_{2k-1}P[t - 2kT_b] \cos(2\pi f_c t) \\ -b_{2k}P[t - 2kT_b] \sin(2\pi f_c t) \\ \text{for } 2kT_b \leq t \leq 2(k+1)T_b \end{cases} \quad (29)$$

where

$$P(t) = \begin{cases} \sqrt{P_p} & 0 \leq t \leq 2T_b \\ 0 & \text{elsewhere.} \end{cases} \quad (30)$$

The autocorrelation is

$$R(t) = P_p \Delta\left(\frac{t}{4T_b}\right) \text{ and } |R(t)|^2 = P_p^2 \Delta^2\left(\frac{t}{4T_b}\right) \quad (31)$$

where we use $R(t)$ to denote the baseband autocorrelation while $R_x(t)$ indicates the autocorrelation of the modulated signal. The PSD of the QPSK is [41]

$$S_x(f) = P_p T_b \text{sinc}^2(2\pi T_b(f + f_c)) + P_p T_b \text{sinc}^2(2\pi T_b(f - f_c)) \quad (32)$$

and the corresponding autocorrelation is defined in (26) with $w = 4T_b$. Because of the Fourier transform pair $\Delta^2\left(\frac{t}{4T_b}\right) \iff \Omega_{2T_b}(\alpha)$, as shown in APPENDIX B, replacing T with $2T_b$, we find the SCSD of the QPSK

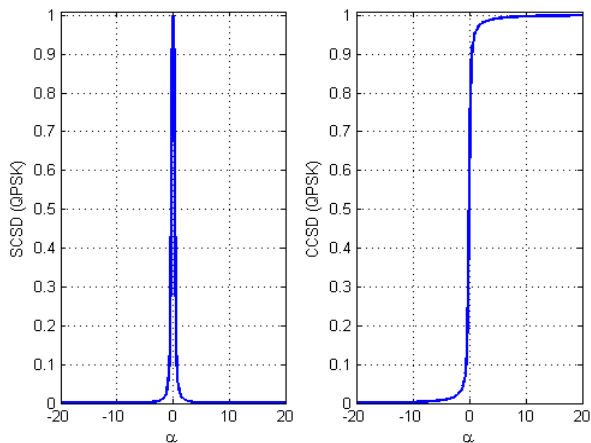
$$\begin{aligned}
 & \frac{1}{2T_b} \sum_n |R_x(t - 2nT_b)|^2 \\
 & \iff Z(\alpha) \\
 & = \frac{P_p^2}{2} \Omega_{2T_b}(\alpha) + \frac{P_p^2}{4} \Omega_{2T_b}(\alpha - 2f_c) + \frac{P_p^2}{4} \Omega_{2T_b}(\alpha + 2f_c). \quad (33)
 \end{aligned}$$

However, using the conjugate autocorrelation, the SCSD of the QPSK is [27]

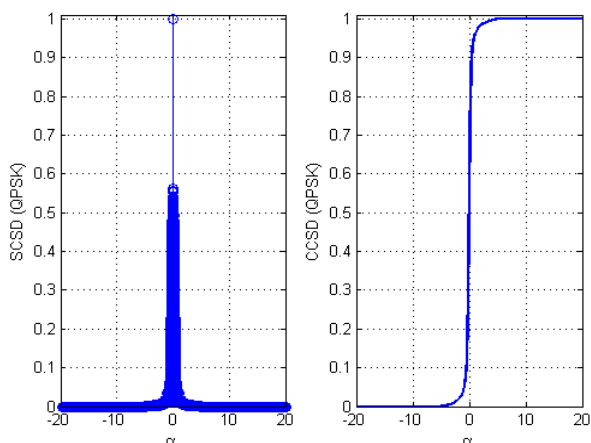
$$Z(\alpha) = \frac{P_p^2}{2} \Omega_{2T_b}(\alpha) \quad (34)$$

where it has been assumed that the in-phase and quadrature components are balanced.

The analytical result of SCSD and CCSD of the QPSK are shown in Fig. 2(a). The SCSD of the QPSK is narrower than that of the BPSK. Hence the transition of the CCSD of the QPSK at the CF is sharper than that of the BPSK. The result comes from the fact that the symbol duration of the QPSK is twice larger than that of the BPSK to maintain the



(a) Analytical result; $f_c = 5R_b$.



(b) Simulated result; $f_s = 20f_c, f_c = 5R_b; T = 500T_s$.

FIGURE 2. SCSD and CCSD of QPSK.

same bit rate, and thereby the signal bandwidth of the QPSK is narrower. The ML detection output of the QPSK is half the signal power squared. The simulation result of the QPSK is shown in Fig. 2(b). The observation interval T is chosen as a 500 symbol time (T_s). The simulated SCSD and CCSD are similar to the corresponding analytical SCSD and CCSD in Fig. 2.

C. OFFSET QUADRATURE PHASE-SHIFT KEYING

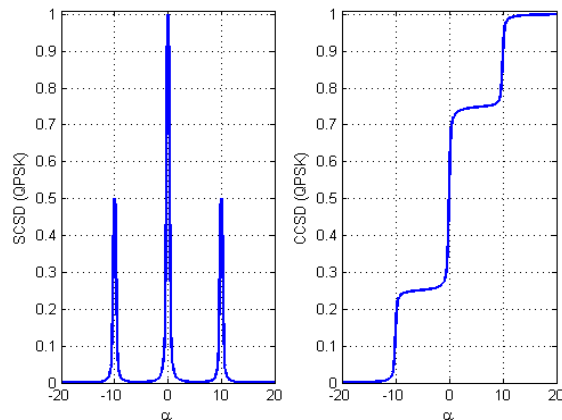
The OQPSK signal can be defined as

$$x_{OQPSK}(t) \tag{35}$$

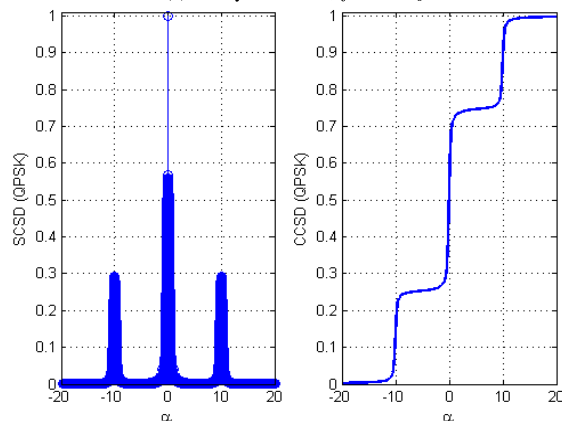
$$= \begin{cases} b_{2k-1}P^I[t - 2kT_b] \cos(2\pi f_c t) \\ -b_{2k-2}P^Q[t - (2k - 2)T_b] \sin(2\pi f_c t) \\ \text{for } (2k - 1)T_b \leq t \leq 2kT_b \\ b_{2k-1}P^I[t - 2kT_b] \cos(2\pi f_c t) \\ -b_{2k}P^Q[t - 2kT_b] \sin(2\pi f_c t) \\ \text{for } 2kT_b \leq t \leq (2k + 1)T_b \end{cases} \tag{36}$$

where

$$P^I(t) = \begin{cases} \sqrt{P_p} & -T_b \leq t \leq T_b \\ 0 & \text{elsewhere} \end{cases} \tag{37}$$



(a) Analytical result; $f_c = 5R_b$.



(b) Simulated result; $f_s = 20f_c, f_c = 5R_b; T = 500T_s$.

FIGURE 3. SCSD and CCSD of OQPSK.

and

$$P^Q(t) = \begin{cases} \sqrt{P_p} & 0 \leq t \leq 2T_b \\ 0 & \text{elsewhere.} \end{cases} \tag{38}$$

The PSD of the OQPSK is the same as the QPSK [42], and the analytical SCSD of the OQPSK can be shown as

$$Z(\alpha) = \frac{P_p^2}{2} \Omega_{2T_b}(\alpha) + \frac{P_p^2}{4} \Omega_{2T_b}(\alpha - 2f_c) + \frac{P_p^2}{4} \Omega_{2T_b}(\alpha + 2f_c) \tag{39}$$

which is identical to (33). The graphical presentation of the SCSD and CCSD of the OQPSK is provided in Fig. 3(a). The simulated SCSD and CCSD of the OQPSK are shown in Fig. 3(b). The result was already predicted in the analysis.

D. MINIMUM SHIFT KEYING

The signal of MSK can be shown as

$$x_{MSK}(t) \tag{40}$$

$$= \begin{cases} b_{2k-1}P^I[t - 2kT_b] \cos(2\pi f_c t) \\ -b_{2k-2}P^Q[t - (2k - 2)T_b] \sin(2\pi f_c t) \\ \text{for } (2k - 1)T_b \leq t \leq 2kT_b \\ b_{2k-1}P^I[t - 2kT_b] \cos(2\pi f_c t) \\ -b_{2k}P^Q[t - 2kT_b] \sin(2\pi f_c t) \\ \text{for } 2kT_b \leq t \leq (2k + 1)T_b \end{cases} \tag{41}$$

where

$$P^I(t) = \begin{cases} \sqrt{2P_p} \cos(\pi t/2T_b) & -T_b \leq t \leq T_b \\ 0 & \text{elsewhere} \end{cases} \quad (42)$$

and

$$P^Q(t) = \begin{cases} \sqrt{2P_p} \sin(\pi t/2T_b) & 0 \leq t \leq 2T_b \\ 0 & \text{elsewhere.} \end{cases} \quad (43)$$

The autocorrelation of the MSK is [42]

$$R(t) = \frac{1}{\pi} \left\{ \pi \Delta\left(\frac{t}{4T_b}\right) \cos\left(\frac{\pi t}{2T_b}\right) + \sin\left(\frac{\pi |t|}{2T_b}\right) \right\} \Pi\left(\frac{t}{4T_b}\right). \quad (44)$$

In APPENDIX C, it is shown that the Fourier transform pair $R(t) \iff \Psi(f)$ and $|R(t)|^2 \iff \Phi(f)$. Therefore the PSD of the MSK is

$$S_x(f) = \frac{P_p}{2} \Psi(f + f_c) + \frac{P_p}{2} \Psi(f - f_c) \quad (45)$$

and its inverse Fourier transform

$$R_x(t) = P_p R(t) \cos(2\pi f_c t). \quad (46)$$

We also find

$$|R_x(t)|^2 = P_p^2 R^2(t) \cos^2(2\pi f_c t) \quad (47)$$

and thereby the SCSD of the MSK can be shown as

$$\begin{aligned} & 2T_b \sum_n |R_x(t - 2nT_b)|^2 \\ & \iff Z(\alpha) \\ & = \frac{P_p^2}{2} \Phi(\alpha) + \frac{P_p^2}{4} \Phi(\alpha + 2f_c) + \frac{P_p^2}{4} \Phi(\alpha - 2f_c). \end{aligned} \quad (48)$$

The corresponding ML detection output can be verified as in (28).

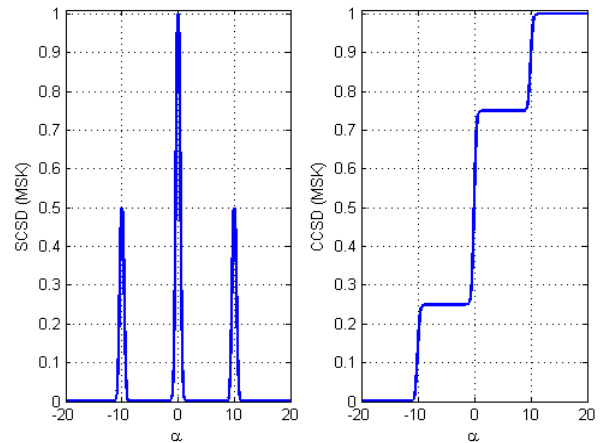
The analytical result of SCSD and CCSD of the MSK are shown in Fig. 4(a). We observe that the SCSD of the MSK was narrower than that of the QPSK (or OQPSK). Hence the transition of the CCSD of the MSK at the CF was sharper. This result comes from the fact that the decay rate of the PSD of the MSK is $1/f^4$, while that of the QPSK or OQPSK is $1/f^2$. Nevertheless the cyclostationary spectrum sensing capability of the MSK can be considered equivalent to that of the OQPSK since the ML detection output is still the square of the received signal power. The simulated result of SCSD and CCSD of the MSK is shown in Fig. 4(b). The transition of the SCSD and CCSD at the CF was acute. We can see that the simulated result of the MSK agreed well with the corresponding analytical result.

E. QUADRATURE AMPLITUDE MODULATION

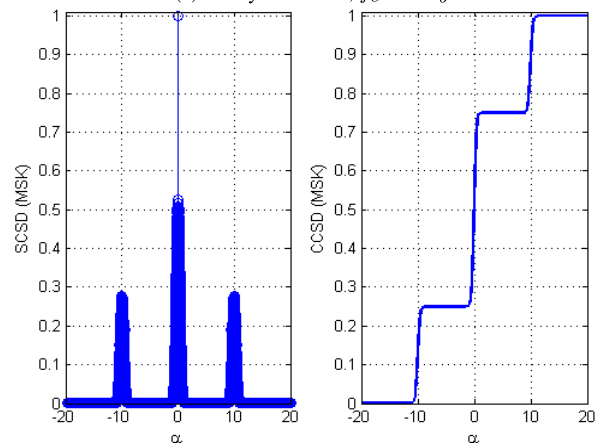
The square QAM signal M -QAM can be expressed as

$$x_{QAM}(t) \quad (49)$$

$$= \begin{cases} d_k^I P[t - kT_s] \cos(2\pi f_c t) \\ -d_k^Q P[t - kT_s] \sin(2\pi f_c t) \\ \text{for } kT_s \leq t \leq (k+1)T_s \end{cases} \quad (50)$$



(a) Analytical result; $f_c = 5R_b$.



(b) Simulated result; $f_s = 20f_c, f_c = 5R_b; T = 500T_s$.

FIGURE 4. SCSD and CCSD of MSK.

where the symbol time $T_s = (\log_2 M)T_b$. The QAM pulse $P(t)$ is defined in as

$$P(t) = \begin{cases} \sqrt{P_q} & 0 \leq t \leq T_s \\ 0 & \text{elsewhere} \end{cases} \quad (51)$$

where P_q is the average power of the QAM pulse. For the M -QAM, the in-phase and quadrature data are $d_k^I, d_k^Q \in \{\pm 1, \pm 3, \pm 5, \dots, \pm(\sqrt{M}-1)\}$. The average power of the M -QAM can be written as [40]

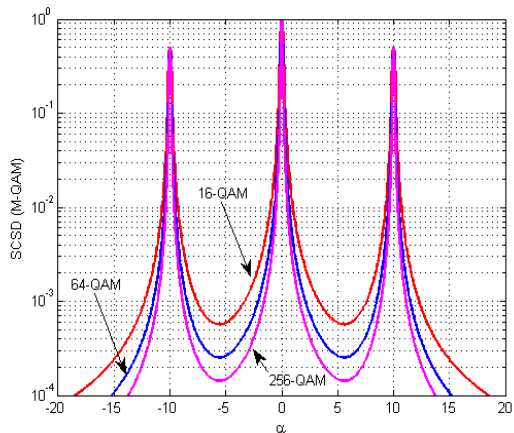
$$P_p = 2 \times \frac{2P_q}{\sqrt{M}} \sum_{k=0}^{(\sqrt{M}-2)/2} (2k+1)^2 = \frac{2(M-1)}{3} P_q \quad (52)$$

$$\text{or } P_q = \frac{3P_p}{2(M-1)} \quad (53)$$

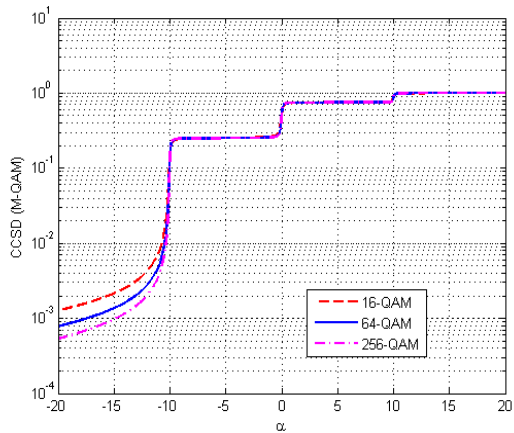
where a factor of 2 is introduced due to scaling from the pulse amplitude modulation (PAM) to the QAM. Therefore, the average autocorrelation of the M -QAM can be shown as

$$R(t) = \frac{4}{\sqrt{M}} \sum_{k=0}^{(\sqrt{M}-2)/2} (2k+1)^2 \frac{1}{T_s} \int_{-\infty}^{\infty} P(s)P(s-t) ds \quad (54)$$

$$= \frac{2(M-1)}{3} P_q \Delta\left(\frac{t}{2T_s}\right) = P_p \Delta\left(\frac{t}{2T_s}\right) \quad (55)$$



(a) SCSD; $f_c = 5R_b$.



(b) CCSD; $f_c = 5R_b$.

FIGURE 5. Analytical SCSD and CCSD of M-QAM.

and

$$|R(t)|^2 = P_p^2 \Delta^2 \left(\frac{t}{2T_s} \right). \quad (56)$$

The Fourier transform pair is shown in APPENDIX B as

$$|R^2(t)|^2 \iff P_p^2 \Omega_{T_s}(f). \quad (57)$$

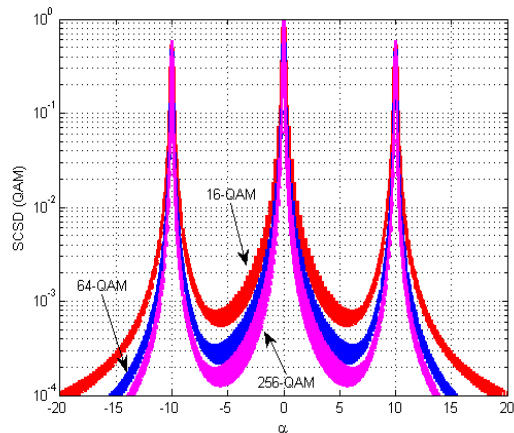
From (55), we can find the PSD of the M -QAM

$$S_x(f) = \frac{P_p T_s}{2} \text{sinc}^2(\pi T_s(f + f_c)) + \frac{P_p T_s}{2} \text{sinc}^2(\pi T_s(f - f_c)) \quad (58)$$

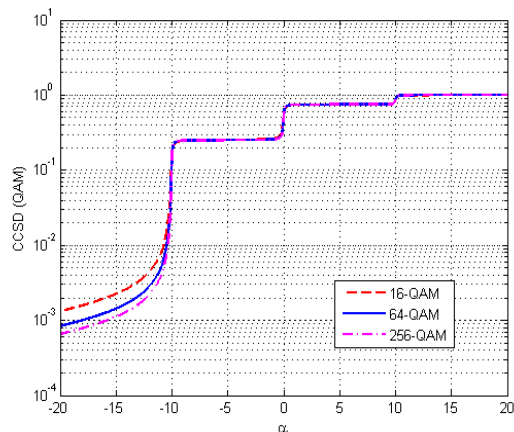
and its inverse Fourier transform $R_x(t)$ defined in (26) with $w = 2T_s$. Hence, we find the SCSD

$$\begin{aligned} & T_s \sum_n |R_x(t - nT_s)|^2 \\ & \iff Z(\alpha) \\ & = \frac{P_p^2}{2} \Omega_{T_s}(\alpha) + \frac{P_p^2}{4} \Omega_{T_s}(\alpha + f_c) + \frac{P_p^2}{4} \Omega_{T_s}(\alpha - f_c) \end{aligned} \quad (59)$$

and the corresponding ML detection output is the same as (28) replacing T_b with T_s . In practice, the signal power of the M -QAM increases by $2(M - 1)/3$ as the signal constellation size M increases to maintain the same bit error rate performance. Consequently, the ML detector outcome of the



(a) SCSD; $f_s = 20 \log_2(M) f_c, f_c = 5R_b; T = 1000T_s$.



(b) CCSD; $f_s = 20 \log_2(M) f_c, f_c = 5R_b; T = 1000T_s$.

FIGURE 6. Simulated SCSD and CCSD of M-QAM.

M -QAM for spectrum sensing becomes larger by a factor of $[2(M - 1)/3]^2$ compared to the QPSK signal. As a result, the cyclostationary spectrum sensing capability enhances for a larger M .

However we show the normalized SCSD and CCSD for easy comparison in Fig. 5 and 6, respectively, with $M = 16, 64,$ and 256 . In fact, the peak value of the SCSD was larger for a larger M although it is not clear in the normalized plot. Nevertheless it is still clear that the cyclic power at the CF ($\alpha = \pm 2f_c$) of the signal was half the signal power at the origin. The analytical SCSD and CCSD are shown in Fig. 5(a) and 5(b), respectively. We can see that the width of the SCSD became narrower as M increased due to the increased symbol time and reduced signal bandwidth. The simulated SCSD and CCSD of the M -QAM are shown in Fig. 6(a) and 6(b), respectively, for $M = 16, 64,$ and 256 . The observation interval was chosen as a 1000 symbol time. The carrier frequency chosen was five times the bit rate, and the sampling rate was $20 \log_2(M)$ times the carrier frequency. The simulation results agreed well with the analytical results although some discrete components of the SCSD were observed in the simulation due to discrete time processing in the simulation. The corresponding CCSD in Fig. 6(b) is rather smooth since the

discrete components were averaged out in the process of the summation. The plots were normalized to the peak values.

IV. CYCLOSTATIONARY DETECTION PERFORMANCE AND POWER HARVESTING

A. DETECTION PERFORMANCE

Consider the received signal $y(t)$ in (10) with the null hypothesis H_0 and the alternative hypothesis H_1 . It can be shown that $y(t)$ contains second order periodicity with frequency α if and only if the CAF [36, (7)]

$$R_y^\alpha(\tau) \triangleq \lim_{T \rightarrow \infty} \frac{1}{T} \int_{-T/2}^{T/2} y\left(t + \frac{1}{2}\tau\right) y\left(t - \frac{1}{2}\tau\right) e^{-j2\pi\alpha t} dt \quad (60)$$

exists and is not identically zero as a function of τ . Note that the author did not take the complex conjugate of $y(t - \tau/2)$ in his original paper, and we followed the same procedure. The cyclic power at the CF α can be obtained as [43]

$$R_y^\alpha(0) = \lim_{T \rightarrow \infty} \frac{1}{T} \int_{-T/2}^{T/2} y^2(t) e^{-j2\pi\alpha t} dt = \lim_{M \rightarrow \infty} \frac{1}{(M+1)T_0} \sum_{m=-M/2}^{M/2} \int_{mT_0-T_0/2}^{mT_0+T_0/2} y^2(t) e^{-j2\pi\alpha t} dt \quad (61)$$

$$= \lim_{M \rightarrow \infty} \frac{1}{(M+1)T_0} \sum_{m=-M/2}^{M/2} \int_{-T_0/2}^{T_0/2} y^2(t + mT_0) e^{-j2\pi\alpha(t+mT_0)} dt \quad (62)$$

with $T = (M+1)T_0$. Since $R_y^\alpha(\tau) \iff S_y^\alpha(f)$ is the Fourier transform pair, we obtain the cyclic power from (7)

$$R_y^\alpha(0) = \int_{-\infty}^{\infty} S_y^\alpha(f) df. \quad (63)$$

In a discrete time signal, we can compute the cyclic power as

$$R_y^\alpha(0) = \frac{1}{(M+1)(N+1)} \times \sum_{m=-M/2}^{M/2} \sum_{n=-N/2}^{N/2} y^2(mT_0 + nT_s) e^{-j2\pi\alpha(nT_s)} \quad (64)$$

where $T_0 = (N+1)T_s$ with the sampling interval T_s . We assume that the cyclic frequency $\alpha = l/T_0$ for a positive integer l . The cyclic power $R_y^\alpha(0)$ is used for power harvesting. Collected values of $R_y^\alpha(0)$ for a time period is convolved to remove residual noise further, and the convolution result is used for spectrum sensing. Note that the unit of the convolution output is $|R_y^\alpha(0)|^2$.

On the other hand, the energy detection can be performed by

$$R_y(0) = \sum_{m=-M/2}^{M/2} \sum_{n=-N/2}^{N/2} y^2(mT_0 + nT_s). \quad (65)$$

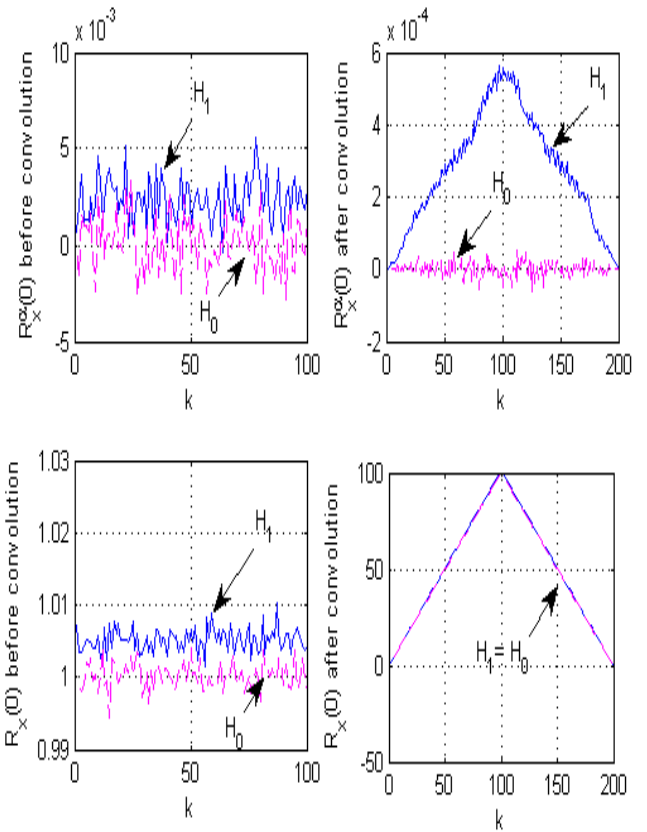


FIGURE 7. CD and ED spectrum sensing output; BPSK; AWGN channel.

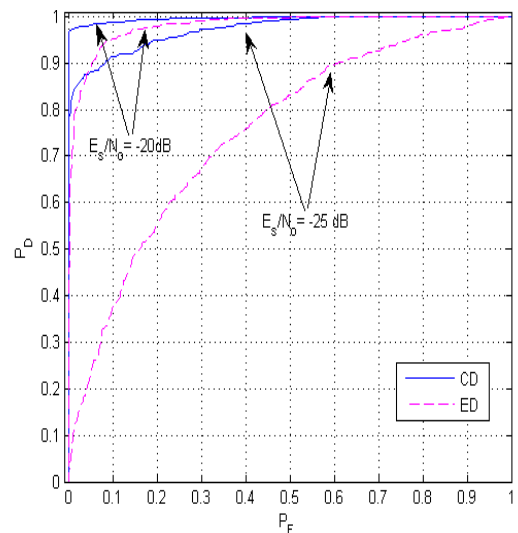


FIGURE 8. Probability of detection and false alarm; BSPK; AWGN channel.

We chose an additive Gaussian noise $\mathcal{N}(0, 1)$, which is a zero mean and unit variance standard Gaussian random variable, in all our simulations. The signal energy-to-noise ratio E_s/N_0 is for each sample. As shown in Fig. 7, we collected 100 detection outputs of the cyclic power $R_y^\alpha(0)$ for CD and the generic power $R_y(0)$ for ED. Under the null hypothesis H_0 , CD has zero mean, and ED has the mean equal to the unit value with the unit noise variance. The simulation

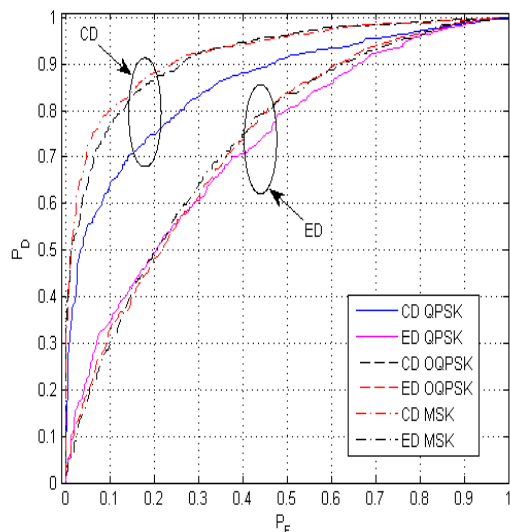


FIGURE 9. Probability of detection and false alarm; Rayleigh fading channel.

results are presented on the left side of Fig. 7. The detection output of CD was convolved to smooth out noise which is represented at the upper right side of the same figure. We can see that the null hypothesis H_0 and the alternative hypothesis H_1 outputs were completely separated from each other, and the difference is obvious. However, H_1 and H_0 convolution results completely overlapped for ED, as can be seen at the lower right side of the figure. Hence, we employed spectrum sensing without convolution for ED and with convolution for CD. For an improvement, we used the center half of the convolution output for CD. The simulation parameters are $E_s/N_o = -20$ dB, $f_s = 8f_c$, $f_s = 64R_b$, $\alpha = 2f_c$, $N = 100$, and $M = 100$.

The BPSK spectrum sensing is shown in Fig. 8 in an AWGN channel in terms of the probability of detection (P_D) and false alarm (P_F). It is apparent that the performance improved at a high SNR. In any case, CD exhibited a better performance than ED. The performance gap between CD and ED became larger at a low SNR, although the performance of ED also improved as the SNR increased. The simulation parameters are $E_s/N_o = -25$ dB and -20 dB, $f_s = 8f_c$, $f_s = 64R_b$, $\alpha = 2f_c$, $N = 100$, and $M = 100$.

We can see a similar performance in QPSK, OQPSK, and MSK in Fig. 9; but QPSK was not as good as OQPSK or MSK. Regarding the QPSK with the balanced in-phase and quadrature components, the cyclic power vanished; and only the generic power could be retrieved [27]. However, our CD, in its nature is more like to obtain the cyclic power separately from in-phase and quadrature. Hence, CD still showed a better performance than ED for QPSK. We maintained the same bit rate and the same SNR for each sample for all three modulation schemes for a fair comparison. Note that the performance of ED displayed the same performance for all cases, which is obviously inferior to CD. The simulation parameters are $E_s/N_o = -25$ dB, $f_s = 4f_s$, $f_s = 32R_b$, $\alpha = 2f_c$, $N = 100$, and $M = 10$.

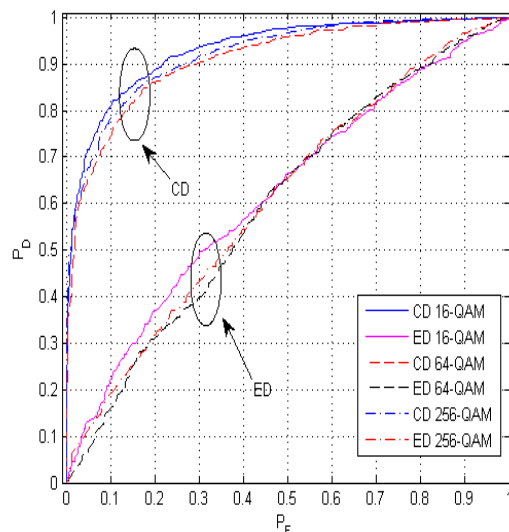


FIGURE 10. Probability of detection and false alarm; Rayleigh fading channel.

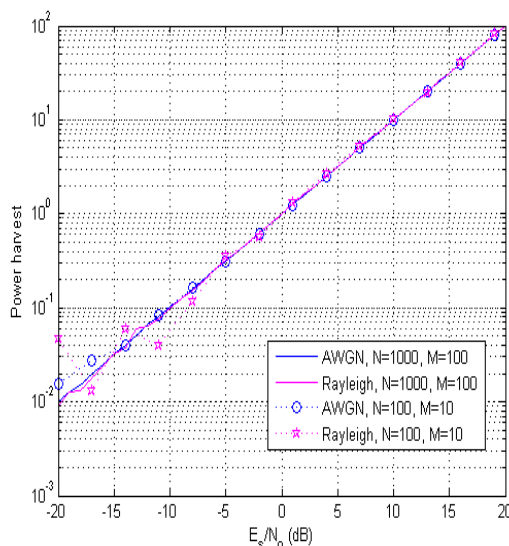


FIGURE 11. Cyclostationary spectrum sensing; BPSK; AWGN and Rayleigh.

The probability of detection and false alarm of M -QAM is shown in Fig. 10. The same average power was employed for all signal constellations for a fair spectrum sensing comparison although this may not have been a good decision in terms of the BER performance. We observed a similar performance for all signal constellations, such as 16-QAM, 64-QAM, and 256-QAM. The signal constellation size of M -QAM did not affect the spectrum sensing capability, whether CD or ED, as long as they have the same average power. However, the performance of CD was significantly improved over the performance of ED. The simulation parameters are $E_s/N_o = -25$ dB, $f_s = 8f_c$, $f_s = 32R_b$, $\alpha = 2f_c$, $N = 100$, and $M = 10$.

B. POWER HARVESTING

Figure 11 displays the power harvest for BPSK with respect to the SNR for each sample. Carriers were scaled by $\sqrt{2}$ to

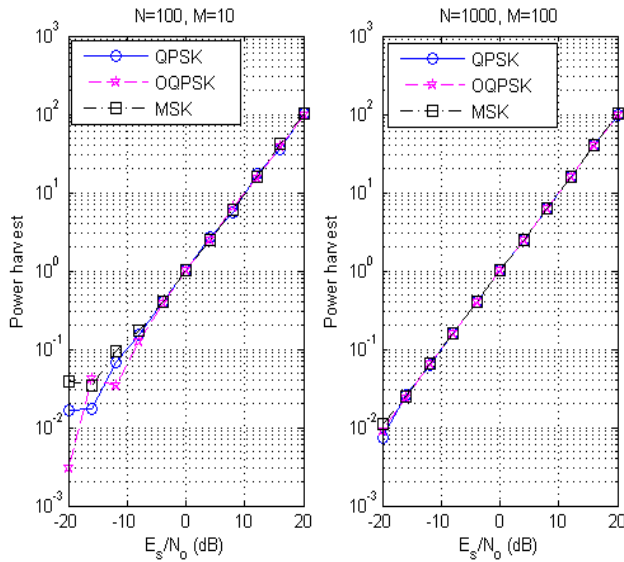


FIGURE 12. Cyclostationary spectrum sensing; Rayleigh fading channel.

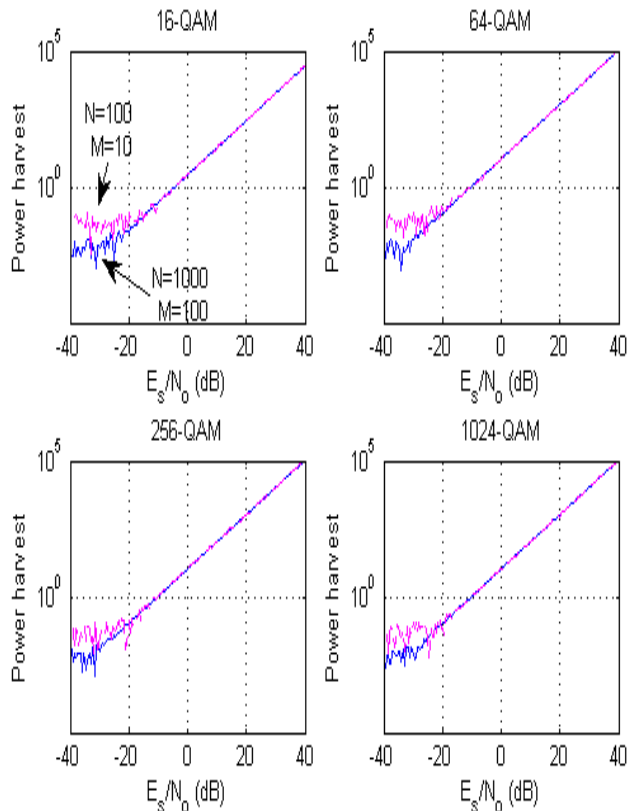


FIGURE 13. Cyclostationary spectrum sensing; QAM; Rayleigh fading channel.

avoid power down by a half. We can see that the signal power of 20 dBW was collected at $E_s/N_o = 20$ dB. At a low SNR, we needed a longer observation time for an accurate power harvesting. For a larger observation interval of $N = 1000$ and $M = 100$, there was hardly any difference between the AWGN channel and fading channel since the average power was the same with and without fading in our simulation.

For a short sensing time of $N = 100$ and $M = 10$, the power harvest in the fading channel was less accurate and deviated from the average signal power, especially at a low SNR. Hence, we can see that a longer harvest time is necessary in fading channels at a low SNR to accurately harvest the cyclic power present in the received signal. In fact, a longer observation interval smooths out the power fluctuation due to fading in the wireless channel. The simulation parameters are $f_s = 8f_c$, $f_c = 8R_b$, and $\alpha = 2f_c$.

The same effect can be observed in Fig. 12 for QPSK, OQPSK, and MSK. The average SNR per sample and data rate were maintained the same for all modulation schemes for a fair comparison. At a low SNR, the power harvest requires a larger harvest time, especially for a fading channel. However, we can see a similar harvest performance of QPSK, OQPSK, and MSK. With a long enough sensing time, the power harvest was still good at an SNR as low as -20 dB. The fading parameters are $f_s = 8f_c$, $f_s = 128R_b$, and $\alpha = 2f_c$.

In Fig. 13, the power harvest of the QAM signal is displayed for different signal constellations. The solid line and dotted line indicate a larger sensing time ($N = 1000$, $M = 100$) and a smaller sensing time ($N = 100$, $M = 10$), respectively. We can still observe an improvement for an SNR below -20 dB with a longer sensing time. For 16-QAM, the harvested power was 40 dBW at an average signal power of 40 dBW or an SNR of 40 dB. (Remember that the noise variance is the unit value in our simulation.) As the signal constellation size increased, the peak-to-average power ratio (PAPR) increased. We can notice the power harvest beyond 40 dBW at an SNR of 40 dB. The simulation parameters are $N = 1000$ and $M = 100$ for solid line, $N = 100$ and $M = 10$ for dotted line, $f_s = 4f_c$, $f_c = 4R_b$, and $\alpha = 2f_c$. Therefore, with the same average power, BPSK, QPSK, OQPSK, and MSK provided the same power harvesting performance. Regarding the QAM with the same average signal power, a larger signal constellation provided a better performance. It is observed that a larger PAPR can exercise a positive influence on power harvesting with cyclostationary spectrum sensing in cognitive radios.

V. CONCLUSION

We developed the ML detection output of cyclostationary detection and showed that the result is equal to the power squared. The sum and cumulation of the CSD were derived for various digital modulation schemes, such as BPSK, QPSK, OQPSK, MSK, and QAM. The ML output was the same as the power squared for all digital modulation schemes. Therefore, it is possible to perform cyclostationary detection with simultaneous power harvest in CR. We provided a simple method of simultaneous cyclostationary spectrum sensing and power harvesting. Corresponding simulation results were illustrated. The method can be useful in 5G cognitive radios with massive MIMO in millimeter-wave frequencies to ameliorate the harmful effect of 5G EMF.

APPENDIXES

APPENDIX A

A PERIODIC AUTOCORRELATION FUNCTION

A periodic autocorrelation function $R_x(t, \tau)$ with a period T_0 can be expressed as

$$R_x(t, \tau) = \sum_n R_x^\alpha(\tau) e^{j2\pi(n/T_0)t} = \sum_\alpha R_x^\alpha(\tau) e^{j2\pi\alpha t} \quad (66)$$

where $\alpha = n/T_0$, and the coefficients of Fourier series

$$R_x^\alpha(\tau) = \frac{1}{T_0} \int_{-T_0/2}^{T_0/2} R_x(t, \tau) e^{-j2\pi\alpha t} dt. \quad (67)$$

Since $R_x(t, \tau)$ is periodic with T_0 , it can be expressed as [34, p. 35, 41] [27, p. 365] [33]

$$R_x(t, \tau) = \lim_{N \rightarrow \infty} \frac{1}{2N+1} \times \sum_{n=-N}^N x(t+nT_0)x(t+nT_0-\tau)^* \quad (68)$$

and with $T = (2N+1)T_0$ [27, P. 362]

$$R_x^\alpha(\tau) = \lim_{T \rightarrow \infty} \frac{1}{T} \int_{-T_0/2}^{T_0/2} \times \sum_{n=-N}^N x(t+nT_0)x(t+nT_0-\tau)^* e^{-j2\pi\alpha t} dt. \quad (69)$$

With a change of a variable $l = t + nT_0$

$$R_x^\alpha(\tau) = \lim_{T \rightarrow \infty} \frac{1}{T} \sum_{n=-N}^N \int_{-T_0/2+nT_0}^{T_0/2+nT_0} \times x(l)x(l-\tau)^* e^{-j2\pi\alpha(l-nT_0)} dl \quad (70)$$

$$= \lim_{T \rightarrow \infty} \frac{1}{T} \int_{-(2N+1)T_0/2}^{(2N+1)T_0/2} x(l)x(l-\tau)^* e^{-j2\pi\alpha l} dl \quad (71)$$

or

$$R_x^\alpha(\tau) = \lim_{T \rightarrow \infty} \frac{1}{T} \int_{-T/2}^{T/2} x(l)x(l-\tau)^* e^{-j2\pi\alpha l} dl. \quad (72)$$

APPENDIX B

FOURIER TRANSFORM PAIR $\Delta^2(t/2T) \iff \Omega_T(f)$

The autocorrelation of the binary polar signal can be written as follows:

$$R(t) = \Delta\left(\frac{t}{2T}\right) \iff S(f) \quad (73)$$

where $S(f)$ is the corresponding PSD. The symbol T can be T_b , $2T_b$, or T_s depending on the modulation scheme; but obviously T is not the observation interval in the main text. The equation (73) can be rewritten as

$$R(t) = \begin{cases} -\frac{t}{T} + 1 & 0 \leq t \leq T \\ \frac{t}{T} + 1 & -T \leq t < 0 \end{cases} \quad (74)$$

or

$$R^2(t) = \Delta^2\left(\frac{t}{2T}\right) = \begin{cases} \frac{t^2}{T^2} - \frac{2t}{T} + 1 & 0 \leq t \leq T \\ \frac{t^2}{T^2} + \frac{2t}{T} + 1 & -T \leq t < 0. \end{cases} \quad (75)$$

We can rewrite (75) as

$$R^2(t) = R_a^2(t) + R_b^2(t) \quad \text{where} \quad (76)$$

$$R_a^2(t) = \frac{t^2}{T^2}, \quad \text{for } |t| \leq T \quad (77)$$

$$R_b^2(t) = 2\Delta\left(\frac{t}{2T}\right) - 1, \quad \text{for } |t| \leq T. \quad (78)$$

The Fourier transform of $R_a^2(t)$ can be expressed as

$$R_a^2(t) \leftrightarrow S_a^2(f) = 2T \operatorname{sinc}(2\pi fT) + \frac{4T \cos(2\pi fT)}{(2\pi fT)^2} - \frac{4T \sin(2\pi fT)}{(2\pi fT)^3} \quad (79)$$

and the Fourier transform of $R_b^2(t)$ as

$$R_b^2(t) \leftrightarrow S_b^2(f) = 2T \operatorname{sinc}^2(\pi fT) - 2T \operatorname{sinc}(2\pi fT). \quad (80)$$

Let us define $\Omega_T(f)$ as the Fourier transform of $R^2(t)$. Then we can see that

$$R^2(t) \leftrightarrow \Omega_T(f) = S(f) \otimes S(f) = S_a^2(f) + S_b^2(f). \quad (81)$$

Therefore

$$\begin{aligned} \Delta^2\left(\frac{t}{2T}\right) &\iff \Omega_T(f) \\ &= 2T \operatorname{sinc}^2(\pi fT) + \frac{4T \cos(2\pi fT)}{(2\pi fT)^2} \\ &\quad - \frac{4T \sin(2\pi fT)}{(2\pi fT)^3}. \end{aligned} \quad (82)$$

In addition, we can note that $\Omega_T(f)$ is bounded since

$$\Omega_T(0) = \int_{-\infty}^{\infty} \Delta^2\left(\frac{t}{2T}\right) dt \quad (83)$$

$$= 2 \int_0^T \left[\frac{t^2}{T^2} - \frac{2t}{T} + 1 \right] dt = \frac{2}{3}T \quad (84)$$

and we also find that

$$\int_{-\infty}^{\infty} \Omega_T(f) df = R_a^2(0) + R_b^2(0) = 0 + 1 = 1 \quad (85)$$

$$\text{or } \int_{-\infty}^{\infty} \Omega_T(f) df = R^2(0) = 1. \quad (86)$$

APPENDIX C

THE SCSD OF MSK

Let us consider the baseband autocorrelation of MSK in (44). The corresponding PSD is

$$\begin{aligned} R(t) \leftrightarrow \Psi(f) &= T_b \operatorname{sinc}^2\left(2\pi T_b(f - 1/4T_b)\right) \\ &\quad + T_b \operatorname{sinc}^2\left(2\pi T_b(f + 1/4T_b)\right) \\ &\quad + \frac{\sin^2\left(2\pi T_b(f + 1/4T_b)\right)}{\pi^2(f + 1/4T_b)} \\ &\quad - \frac{\sin^2\left(2\pi T_b(f - 1/4T_b)\right)}{\pi^2(f - 1/4T_b)}. \end{aligned} \quad (87)$$

On the other hand, the square of the autocorrelation can be written as

$$|R(t)|^2 = \frac{1}{\pi^2} \left\{ \pi^2 \Delta^2 \left(\frac{t}{4T_b} \right) \cos^2 \left(\frac{\pi t}{2T_b} \right) + \sin^2 \left(\frac{\pi |t|}{2T_b} \right) + 2\pi \Delta \left(\frac{t}{4T_b} \right) \cos \left(\frac{\pi t}{2T_b} \right) \sin \left(\frac{\pi |t|}{2T_b} \right) \right\} \Pi \left(\frac{t}{4T_b} \right) \quad (88)$$

or

$$|R(t)|^2 = \frac{1}{2\pi^2} \left\{ \pi^2 \Delta^2 \left(\frac{t}{4T_b} \right) \left[1 + \cos \left(\frac{2\pi t}{2T_b} \right) \right] + \left[1 - \cos \left(\frac{2\pi t}{2T_b} \right) \right] \right\} \Pi \left(\frac{t}{4T_b} \right) + \frac{2}{\pi} \Delta \left(\frac{t}{4T_b} \right) \cos \left(\frac{\pi t}{2T_b} \right) \sin \left(\frac{\pi |t|}{2T_b} \right). \quad (89)$$

The expression can be divided into two terms

$$|R(t)|^2 = |R(t)|_a^2 + |R(t)|_b^2 \quad (90)$$

where we define

$$|R(t)|_a^2 \triangleq \frac{1}{2\pi^2} \left\{ \pi^2 \Delta^2 \left(\frac{t}{4T_b} \right) \left[1 + \cos \left(\frac{2\pi t}{2T_b} \right) \right] + \left[1 - \cos \left(\frac{2\pi t}{2T_b} \right) \right] \right\} \text{rect} \left(\frac{t}{4T_b} \right) \quad (91)$$

and

$$|R(t)|_b^2 \triangleq \frac{2}{\pi} \Delta \left(\frac{t}{4T_b} \right) \cos \left(\frac{\pi t}{2T_b} \right) \sin \left(\frac{\pi |t|}{2T_b} \right). \quad (92)$$

The corresponding Fourier transforms are

$$\begin{aligned} |R(t)|_a^2 &\iff \Phi_a(f) \\ &= \frac{1}{2} \Omega_{2T_b}(\alpha) + \frac{1}{4} \Omega_{2T_b}(\alpha - 1/2T_b) \\ &\quad + \frac{1}{4} \Omega_{2T_b}(\alpha + 1/2T_b) \\ &\quad + \frac{2T_b}{\pi^2} \text{sinc}(4\pi f T_b) - \frac{T_b}{\pi^2} \text{sinc}(4\pi(f - 1/2T_b)T_b) \\ &\quad - \frac{T_b}{\pi^2} \text{sinc}(4\pi(f + 1/2T_b)T_b) \end{aligned} \quad (93)$$

and

$$\begin{aligned} |R(t)|_b^2 &\iff \Phi_b(f) \\ &= -\frac{1}{2\pi^2 \left[f - \frac{1}{2T_b} \right]} \cos \left(4\pi T_b \left[f - \frac{1}{2T_b} \right] \right) \\ &\quad + \frac{1}{8\pi^3 T_b \left[f - \frac{1}{2T_b} \right]^2} \sin \left(4\pi T_b \left[f - \frac{1}{2T_b} \right] \right) \\ &\quad + \frac{1}{2\pi^2 \left[f + \frac{1}{2T_b} \right]} \cos \left(4\pi T_b \left[f + \frac{1}{2T_b} \right] \right) \\ &\quad - \frac{1}{8\pi^3 T_b \left[f + \frac{1}{2T_b} \right]^2} \sin \left(4\pi T_b \left[f + \frac{1}{2T_b} \right] \right) \\ &\quad - \frac{1}{\pi^2 \left[f - \frac{1}{2T_b} \right]} \left[\sin^2 \left(2\pi T_b \left[f - \frac{1}{2T_b} \right] \right) \right] \\ &\quad + \frac{1}{\pi^2 \left[f + \frac{1}{2T_b} \right]} \left[\sin^2 \left(2\pi T_b \left[f + \frac{1}{2T_b} \right] \right) \right]. \end{aligned} \quad (94)$$

Finally

$$|R(t)|^2 \iff \Phi(f) = \Phi_a(f) + \Phi_b(f). \quad (95)$$

From (88) we observe

$$\int_{-\infty}^{\infty} \Phi(f) df = |R(0)|^2 = 1 \quad (96)$$

or from (91) and (92)

$$\begin{aligned} \int_{-\infty}^{\infty} \Phi(f) df &= \int_{-\infty}^{\infty} \Phi_a(f) df + \int_{-\infty}^{\infty} \Phi_b(f) df \\ &= |R(0)|_a^2 + |R(0)|_b^2 = 1 + 0 = 1. \end{aligned} \quad (97)$$

REFERENCES

- [1] Y.-H. Lee, A.-S. Wang, Y.-D. Liao, T.-W. Lin, Y.-J. Chi, C.-C. Wong, N. Shinohara, Q. Yuan, and Q. Chen, "Wireless power IoT system using polarization switch antenna as polling protocol for 5G mobile network," in *Proc. IEEE Wireless Power Transf. Conf. (WPTC)*, May 2017, pp. 1–3.
- [2] Z. Chu, F. Zhou, Z. Zhu, R. Q. Hu, and P. Xiao, "Wireless powered sensor networks for Internet of Things: Maximum throughput and optimal power allocation," *IEEE Internet Things J.*, vol. 5, no. 1, pp. 310–321, Feb. 2018.
- [3] X. Zhang, X. Zhang, and L. Han, "An energy efficient Internet of Things network using restart artificial bee colony and wireless power transfer," *IEEE Access*, vol. 7, pp. 12686–12695, 2019.
- [4] M. Sinaie, P.-H. Lin, A. Zappone, P. Azmi, and E. A. Jorswieck, "Delay-aware resource allocation for 5G wireless networks with wireless power transfer," *IEEE Trans. Veh. Technol.*, vol. 67, no. 7, pp. 5841–5855, Jul. 2018.
- [5] D. Zhai, R. Zhang, J. Du, Z. Ding, and F. R. Yu, "Simultaneous wireless information and power transfer at 5G new frequencies: Channel measurement and network design," *IEEE J. Sel. Areas Commun.*, vol. 37, no. 1, pp. 171–186, Jan. 2019.
- [6] T. D. P. Perera, D. N. K. Jayakody, S. K. Sharma, S. Chatzinotas, and J. Li, "Simultaneous wireless information and power transfer (SWIPT): Recent advances and future challenges," *IEEE Commun. Surveys Tuts.*, vol. 20, no. 1, pp. 264–302, 1st Quart., 2018.
- [7] R. Zhang and C. K. Ho, "MIMO broadcasting for simultaneous wireless information and power transfer," *IEEE Trans. Wireless Commun.*, vol. 12, no. 5, pp. 1989–2001, May 2013.
- [8] T. Aoki, Q. Yuan, D. Quang-Thang, M. Okada, and H.-M. Hsu, "Maximum transfer efficiency of MIMO-WPT system," in *Proc. IEEE Wireless Power Transf. Conf. (WPTC)*, Jun. 2018, pp. 1–3.
- [9] X. Liu, X. Zhang, M. Jia, L. Fan, W. Lu, and X. Zhai, "5G-based green broadband communication system design with simultaneous wireless information and power transfer," *Phys. Commun.*, vol. 28, pp. 130–137, Jun. 2018.
- [10] X. Liu, F. Li, and Z. Na, "Optimal resource allocation in simultaneous cooperative spectrum sensing and energy harvesting for multichannel cognitive radio," *IEEE Access*, vol. 5, pp. 3801–3812, 2017.
- [11] H. Hu, X. Da, L. Ni, Y. Huang, and H. Zhang, "Green energy powered cognitive sensor network with cooperative sensing," *IEEE Access*, vol. 7, pp. 17354–17364, 2019.
- [12] H. Hosseini, A. Anpalagan, K. Raahemifar, S. Erkucuk, and S. Habib, "Joint wavelet-based spectrum sensing and FBMC modulation for cognitive mmWave small cell networks," *IET Commun.*, vol. 10, no. 14, 2016, pp. 1803–1809.
- [13] J. Lu, D. Steinbach, P. Cabrol, and P. Pietraski, "Modeling the impact of human blockers in millimeter wave radio links," *ZTE Commun. Mag.*, vol. 10, no. 4, pp. 23–28, 2012.
- [14] M. Jin, Q. Guo, Y. Li, J. Xi, and Y. Yu, "Energy detection with random arrival and departure of primary signals: New detector and performance analysis," *IEEE Trans. Veh. Technol.*, vol. 66, no. 11, pp. 10092–10101, Nov. 2017.
- [15] S. Haykin, "Cognitive radio: Brain-empowered wireless communications," *IEEE J. Sel. Areas Commun.*, vol. 23, no. 2, pp. 201–220, Feb. 2005.
- [16] A. Mariani, A. Giorgetti, and M. Chiani, "Effects of noise power estimation on energy detection for cognitive radio applications," *IEEE Trans. Commun.*, vol. 59, no. 12, pp. 3410–3420, Dec. 2011.

- [17] X. Kang, Y.-C. Liang, A. Nallanathan, H. K. Garg, and R. Zhang, "Optimal power allocation for fading channels in cognitive radio networks: Ergodic capacity and outage capacity," *IEEE Trans. Wireless Commun.*, vol. 8, no. 2, pp. 940–950, Feb. 2009.
- [18] K.-L. Du and W. H. Mow, "Affordable cyclostationarity-based spectrum sensing for cognitive radio with smart antennas," *IEEE Trans. Veh. Technol.*, vol. 59, no. 4, pp. 1877–1886, May 2010.
- [19] V. Prithiviraj, B. Sarankumar, A. Kalaiyarasan, P. P. Chandru, and N. N. Singh, "Cyclostationary analysis method of spectrum sensing for cognitive radio," in *Proc. 2nd Int. Conf. Wireless Commun., Veh. Technol., Inf. Theory Aerosp. Electron. Syst. Technol.*, 2011, pp. 1–5.
- [20] M. Derakhshani, T. Le-Ngoc, and M. Nasiri-Kenari, "Efficient cooperative cyclostationary spectrum sensing in cognitive radios at low SNR regimes," *IEEE Trans. Wireless Commun.*, vol. 10, no. 11, pp. 3754–3764, Nov. 2011.
- [21] A. V. Dandawate and G. B. Giannakis, "Statistical tests for presence of cyclostationarity," *IEEE Trans. Signal Process.*, vol. 42, no. 9, pp. 2355–2369, Sep. 1994.
- [22] A. Al-Habashna, O. A. Dobre, R. Venkatesan, and D. C. Popescu, "Second-order cyclostationarity of mobile WiMAX and LTE OFDM signals and application to spectrum awareness in cognitive radio systems," *IEEE J. Sel. Topics Signal Process.*, vol. 6, no. 1, pp. 26–42, Feb. 2012.
- [23] W. M. Jang, "Blind cyclostationary spectrum sensing in cognitive radios," *IEEE Commun. Lett.*, vol. 18, no. 3, pp. 393–396, Mar. 2014.
- [24] J. Lunden, V. Koivunen, A. Huttunen, and H. V. Poor, "Collaborative cyclostationary spectrum sensing for cognitive radio systems," *IEEE Trans. Signal Process.*, vol. 57, no. 11, pp. 4182–4195, Nov. 2009.
- [25] C. M. Spooner, "Higher-order statistics for nonlinear processing of cyclostationary signals," in *Cyclostationarity in Communications and Signal Processing*. Piscataway, NJ, USA: IEEE Press, 1994, ch. 2.
- [26] J.-C. Shen and E. Alsusa, "An efficient multiple lags selection method for cyclostationary feature based spectrum-sensing," *IEEE Signal Process. Lett.*, vol. 20, no. 2, pp. 133–136, Feb. 2013.
- [27] W. Gardner, *Statistical Spectral Analysis: A Nonprobabilistic Theory*. Englewood Cliffs, NJ, USA: Prentice-Hall, 1988.
- [28] S. Sasipriya and R. Vigneshram, "An overview of cognitive radio in 5G wireless communications," in *Proc. IEEE Int. Conf. Comput. Intell. Comput. Res. (ICCCIC)*, Dec. 2016, pp. 1–5.
- [29] A. Ö. Ercan, M. O. Sunday, and I. F. Akyildiz, "RF energy harvesting and transfer for spectrum sharing cellular IoT communications in 5G systems," *IEEE Trans. Mobile Comput.*, vol. 17, no. 7, pp. 1680–1694, Jul. 2018.
- [30] H. Al-Hraishawi and G. A. Aruma Baduge, "Wireless energy harvesting in cognitive massive MIMO systems with underlay spectrum sharing," *IEEE Wireless Commun. Lett.*, vol. 6, no. 1, pp. 134–137, Feb. 2017.
- [31] *Scientists Warn of Potential Serious Health Effects of 5G*. Accessed: Mar. 20, 2020. [Online]. Available: <https://www.5gappeal.eu/the-5g-appeal/>
- [32] W. Gardner, "Common pitfalls in the application of stationary process theory to time-sampled and modulated signals," *IEEE Trans. Commun.*, vol. 35, no. 5, pp. 529–534, May 1987.
- [33] W. A. Gardner, A. Napolitano, and L. Paura, "Cyclostationarity: Half a century of research," *Signal Process.*, vol. 86, pp. 639–697, Apr. 2006.
- [34] W. A. Gardner, "An introduction to cyclostationary signals," in *Cyclostationarity in Communications and Signal Processing*. Piscataway, NJ, USA: IEEE Press, 1994, ch. 1.
- [35] W. Gardner, "The role of spectral correlation in design and performance analysis of synchronizers," *IEEE Trans. Commun.*, vol. 34, no. 11, pp. 1089–1095, Nov. 1986.
- [36] W. A. Gardner, "The spectral correlation theory of cyclostationary time-series," *Signal Process.*, vol. 11, no. 4, p. 405, Dec. 1986.
- [37] W. A. Gardner and C. M. Spooner, "Signal interception: Performance advantages of cyclic-feature detectors," *IEEE Trans. Commun.*, vol. 40, no. 1, pp. 149–159, Jan. 1992.
- [38] W. A. Gardner, "Signal interception: A unifying theoretical framework for feature detection," *IEEE Trans. Commun.*, vol. 36, no. 8, pp. 897–906, Aug. 1988.
- [39] E. Rebeiz, P. Urriza, and D. Cabric, "Optimizing wideband cyclostationary spectrum sensing under receiver impairments," *IEEE Trans. Signal Process.*, vol. 61, no. 15, pp. 3931–3943, Aug. 2013.
- [40] B. P. Lathi and Z. Ding, *Modern Digital and Analog Communication Systems*, 4th ed. New York, NY, USA: Oxford Univ. Press, 2009.
- [41] T. S. Rappaport, *Wireless Communications: Principles and Practice*, 2nd ed. Upper Saddle River, NJ, USA: Prentice-Hall, 2002.
- [42] S. Gronemeyer and A. McBride, "MSK and offset QPSK modulation," *IEEE Trans. Commun.*, vol. COM-24, no. 8, pp. 809–820, Aug. 1976.
- [43] Y. Liu, Z. Zhong, G. Wang, and D. Hu, "Cyclostationary detection based spectrum sensing for cognitive radio networks," *J. Commun.*, vol. 10, no. 1, pp. 74–79, Jan. 2015.



WON MEE JANG received the B.A. degree in computer science from the University of Minnesota, Minneapolis, MN, USA, in 1984, the M.S. degree in computer engineering from George Mason University, Fairfax, VA, USA, in 1987, and the D.Sc. degree in electrical engineering from The George Washington University, Washington, DC, USA, in 1996. From 1988 to 1991, she was with the Information and Electronics Division, Korea Research Institute of Science and Technology, Pohang, South Korea. From 1995 to 1998, she was a Wireless Engineer with Comsearch, Ashburn, VA, USA. Since 1998, she has been with the Department of Computer and Electrical Engineering, University of Nebraska–Lincoln, Lincoln, NE, USA, where she is currently an Associate Professor. Her research interests include spread spectrum, satellite communications, global navigation satellite systems, code division multiple access, orthogonal frequency division multiplexing, MIMO, mmWave communication, cognitive radios, and communication theory.

• • •